Nanoscale

PAPER

View Article Online
View Journal | View Issue

Cite this: *Nanoscale*, 2019, **11**, 6368

Broad-band high-gain room temperature photodetectors using semiconductor–metal nanofloret hybrids with wide plasmonic response†

Amir Ziv,[a] Avra Tzaguy,[b] Zhiyuan Sun,[c] Shira Yochelis,[a] Emmanuel Stratakis,[d] George Kenanakis,[d] George C. Schatz,[e] Lincoln J. Lauhon,[c] David N. Seidman,[c,f] Yossi Paltiel*[a] and Roie Yerushalmi*[b]

Semiconducting nanowires are widely studied as building blocks for electro-optical devices; however, their limited cross-section and hence photo-response hinder the utilization of their full potential. Herein, we present an opto-electronic device for broad spectral detection ranging from the visible (VIS) to the short wavelength infra-red (SWIR) regime, using SiGe nanowires coupled to a broadband plasmonic antenna. The plasmonic amplification is obtained by deposition of a metallic nanotip at the edge of a nanowire utilizing a bottom-up synthesis technique. The metallic nanotip is positioned such that both optical plasmonic modes and electrical detection paths are coupled, resulting in a specific detectivity improvement of ~1000 compared to conventional SiGe NWs. Detectivity and high gain are also measured in the SWIR regime owing to the special plasmonic response. Furthermore, the temporal response is improved by ~1000. The fabrication process is simple and scalable, and it relies on low-resolution and facile fabrication steps with minimal requirements for top-down techniques.

Received 13th January 2019,
Accepted 28th February 2019

DOI: 10.1039/c9nr00385a

rsc.li/nanoscale

Introduction

Semiconducting nanowires (NWs) hold major promise for nano-electronics[1] and photodetectors in particular[2–4] thanks to their nanometric confinement in two-dimensions. The high geometrical aspect ratio of NWs, typically in the range of 100 to 1000, enables bridging over the nanometer-micron scales, which is central for the facile fabrication of contact electrodes, while benefitting from the nanometric dimensionality of the NW building blocks. In many nano-scale photodetectors the active area is located at the interface between the NW and a metal electrode.[5,6] In this case, the junction's cross-section is, however, very small, minimizing the external quantum efficiency of the detector. Several strategies have been demonstrated to overcome the limited light absorption cross-section of NWs, including exploiting an internal photoelectric gain (g), such that each absorbed photon is transformed to many electrons.[7] Because of the dark current and noise amplification it is desirable that the gain mechanism is activated under illumination to enhance the overall signal-to-noise (S/N) ratio. In many semiconductor NW photodetectors, the presence of surface traps dominates electrical conduction and photoresponse,[6–11] which causes a large gain under illumination, resulting from the large ratio between the excited photo-carriers' lifetime and their transient time. This comes, however, with the price of slow response times whereas the same gain mechanism also operates for thermal excitation.

Another strategy to achieve gain in electro-optical nanowire devices relies on coupling surface plasmon polaritons (SPPs), typically obtained by metallic structures positioned in proximity to the semiconducting NWs.[12,13] The highly localized SPP enhanced electric fields amplify the light collection efficiency and therefore permit photoelectric detection. However, this approach requires advanced lithography techniques,[9] and SPPs are not easily coupled to free-space radiation. Nevertheless, the use of plasmonics in photodetection schemes is highly beneficial because the metallic structure can simultaneously function as a plasmonic antenna,[14] or an

[a]*Department of Applied Physics, the Hebrew University, Jerusalem, Edmond J. Safra Campus, Givat Ram, Jerusalem, 91904, Israel. E-mail: yossi.paltiel@mail.huji.ac.il*
[b]*Institute of Chemistry and the Center for Nanoscience and Nanotechnology, the Hebrew University of Jerusalem, Edmond J. Safra Campus, Givat Ram, Jerusalem, 91904, Israel. E-mail: roie.yerushalmi@mail.huji.ac.il*
[c]*Department of Materials Science and Engineering, Northwestern University, 2220 Campus Drive, Evanston60208-3108, USA*
[d]*Institute of Electronic Structure and Laser (IESL), Foundation for Research & Technology-Hellas (FORTH), N. Plastira 100, GR-70013 Heraklion, Crete, Greece*
[e]*Department of Chemistry, Northwestern University, Evanston, 60208-3113, USA*
[f]*Northwestern University Center for Atom-Probe Tomography (NUCAPT), 2220 Campus Drive, Evanston, 60208-3108, USA*

† Electronic supplementary information (ESI) available: Additional experimental details and simulation results. See DOI: 10.1039/c9nr00385a

amplifier, and an electrical contact,[15] and applications are not solely limited to photodetection but also to the fields of surface enhanced Raman spectroscopy (SERS),[16,17] tip enhanced Raman spectroscopy (TERS),[18] molecular vibration spectrscopy,[19] molecular electronics,[20] gain medium[21] and light harvesting.[22] Furthermore, earlier studies demonstrated that coupling between a plasmonic metal nanostructure, which permits development of a localized plasmonic resonance (LSPR), and a semiconductor, allows NIR photodetection based on hot electrons[23–28] or charge separation.[29] The LSPR can be efficiently coupled to free-space radiation, an advantage for the fabrication of simple detectors, so it is highly desirable to extend this ability so that cooling the detector isn't required for high performance in the NIR and SWIR regimes. Additional requirements from some devices are the ability to miniaturize the detector to several nanometers, while controlling the exact morphology and size of the plasmonic structure, having a strong coupling to the semiconductor and using simple and scalable fabrication schemes.

Thus, applying the concept of coupling a LSPR and a semiconductor NW is highly desirable, since it permits both miniaturization to the nanoscale and, as demonstrated below, room-temperature operation. Furthermore, Ge NWs have been shown to have a resonant field enhancement, which can be engineered to work in the IR regime.[30] However, to exploit fully the potential of this phenomenon the issue of photoresponse speed also needs to be addressed.

Herein, we present a device concept for a semiconductor–metal nano-floret hybrid (Au-NF) based photodetection, where localized surface plasmon resonances (LSPR) in the VIS-NIR-SWIR regime are coupled strongly to a semiconductor channel. This unique NW is synthesized using a simple self-processing synthesis and later assembled into a device using a self-organization technique. Therefore, all the above-mentioned requirements for a plasmonic-semiconductor photodetector are fulfilled. The plasmonic metallic nanostructure is located at the edge of the NW, such that not only a plasmonic gain is achieved but a tunneling junction exists at the bottleneck of the electrical junction. Our results demonstrate that this junction improves dramatically the response time, while the strong localized plasmonic-field enhances mainly the detector's quantum efficiency. The unique Au-NF metallic–semiconducting hybrid structure yields a broad plasmonic response through the SWIR regime. The spectral range of the plasmonic response can be tuned by the Au-NF structure's parameters (*e.g.* NW diameter and metal nanotip deposition morphology). Electromagnetic (EM) numerical simulations support the experimental data. All the above is achieved by scalable and fast fabrication techniques, which makes this device concept suitable for many applications.

Results and discussion

The device concept is presented in Fig. 1a and b; the NW with a gold nanotip, termed a nano-floret (NF),[31] is suspended between two micron-scale metal electrodes and the electrical junction is achieved at the contact between the gold nanotip and the counter electrode. The fabrication process is described in detail elsewhere,[32] briefly, two micron-scale metal electrodes are fabricated using conventional photolithography techniques, with a micron-scale separation. Next, gold nanoparticles are selectively adsorbed only on one electrode and transferred to a chemical vapor deposition (CVD) system, where SiGe nanowires are grown by the vapor–liquid–solid (VLS) mechanism. Lastly, gold is deposited only at the edge of the NW by a simple, self-terminated wetting process (details elsewhere[31]). We emphasize strongly that the described process is robust, fast and scalable, and results in a compact *on chip* device, which can be integrated readily into larger circuits or into a sensor array.[32] All measurements were performed on two types of devices: (1), a NF device, with a unique NW structure; and (2) a control NW device, with an unmodified NW. A comparison between the illustrations of the two types of NWs is presented in Fig. 1c.

The device photo-response was tested by applying a DC electrical bias across the junction, illuminating it with a CW laser, and measuring the change in the resulting electrical current (see the ESI† for more information and current–voltage characteristics of the devices).

The photoelectric gain (g), is defined as the ratio between the number of photoelectric carriers I_{ph}/e and absorbed photons $\eta P_{opt}/h\nu$, implying: $g = \frac{I_{ph}/e}{\eta P_{opt}/h\nu}$. This, in addition to the typical figure of merit, the specific detectivity, permits an estimation of the quality and efficiency of the photodetector. A comparison between the specific detectivity (D^*) and photoelectric gain (g) of typical devices is displayed in Fig. 2a. It is apparent that the NF-based devices exhibit higher D^* and g values compared to the respective NW devices. Also, the photoresponse of the NW devices vanishes at 660 nm and longer wavelengths, for our measurement setup's sensitivity, while the NF device's response is clear in the NIR regime, that is, at 785 nm and 1064 nm. Notably, the D^* and g values in the UV regime (405 nm) are significantly higher compared to the other measured wavelengths (532 nm–1850 nm), which we ascribe to different photo-response mechanisms; at 405 nm, the photoresponse seems to be the results of trapped surface states, whereas at other wavelengths the photoresponse is related to the localized plasmon. This difference can also be seen by inspecting the photocurrent dependence on the optical power shown in Fig. 2b. At 405 nm, the dependence is non-linear reaching saturation, while for 785 nm the dependence remains linear. As will be discussed later, the non-linear photocurrent dependence is attributed to complete trapping of all surface states at higher optical powers, which also explain the high D^* and g values due to the large ratio between the trapped electron lifetime and the corresponding hole transient time. This mechanism is beneficial but hard to control. Notably, for different NF devices, the maximum photoresponse is measured at different wavelengths, which can be attributed to slight variations in the shape and size of the NF gold nanoshell tip for specific devices (see Fig. S6 in the ESI†).

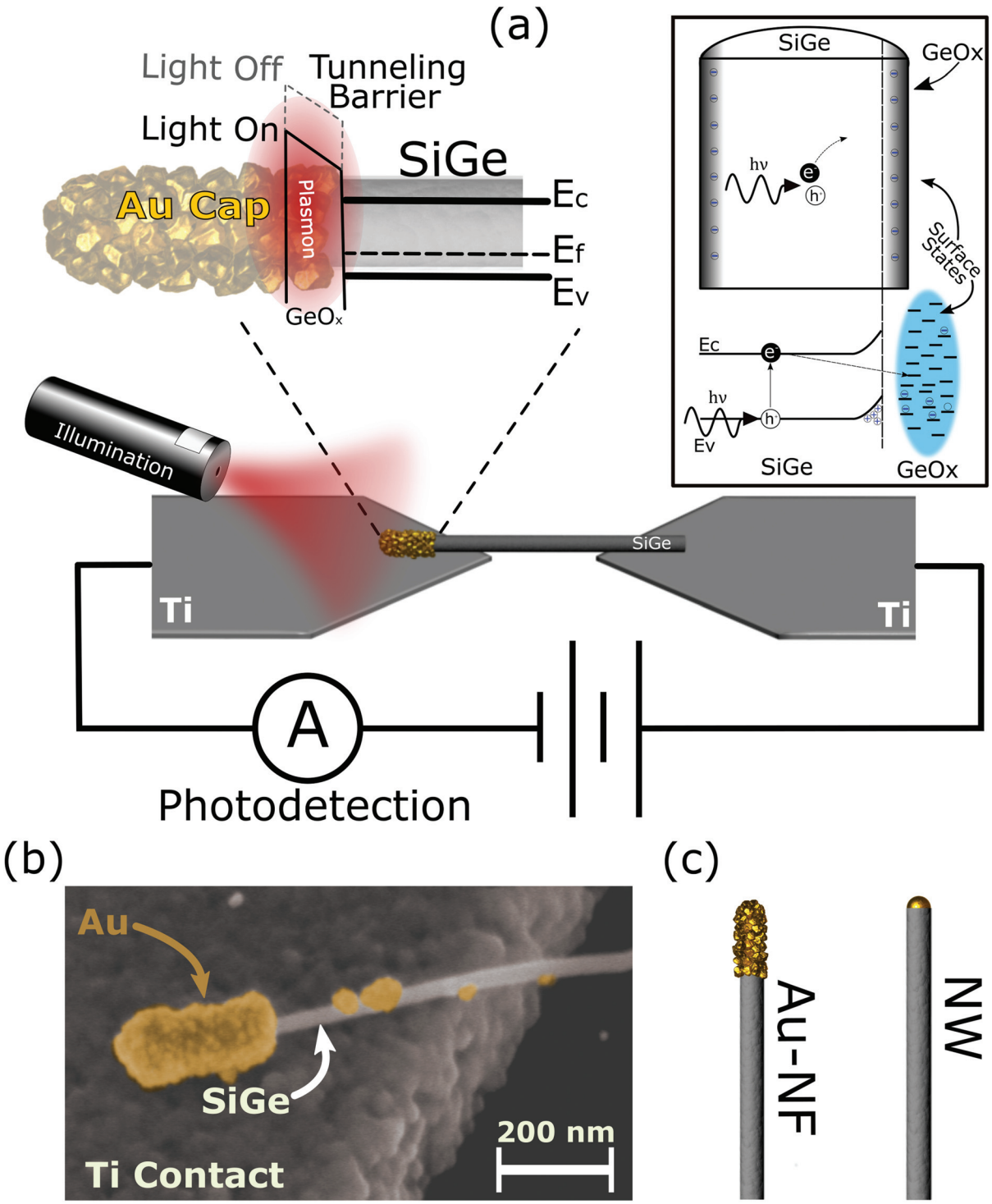

Fig. 1 (a) Nano-floret photodetector device concept: a SiGe nanowire with a nanoshell gold nanotip is suspended between two metal contacts, which are connected to an external bias and a current measuring device. Upon illumination, a localized plasmonic resonance of the gold shell effectively lowers the tunneling barrier between the SC and the gold nanotip. Upper right inset: Surface traps are located at the GeO_2 layers, where an electron–hole pair is created upon illumination, the electron drifts and is captured in the surface states, while an additional hole is added to the valence band, contributing to the conductance. (b) SEM image of the Au-NF-electrode area, where the Au-NF, with the gold nanotip, the SiGe NW and Ti contact are displayed in color for presentation clarity. (c) Schematic diagrams of an Au-NF with a deposited metallic nanotip and a SiGe NW with a small gold nanoparticle at the edge of the NW, which was obtained through the CVD synthesis.

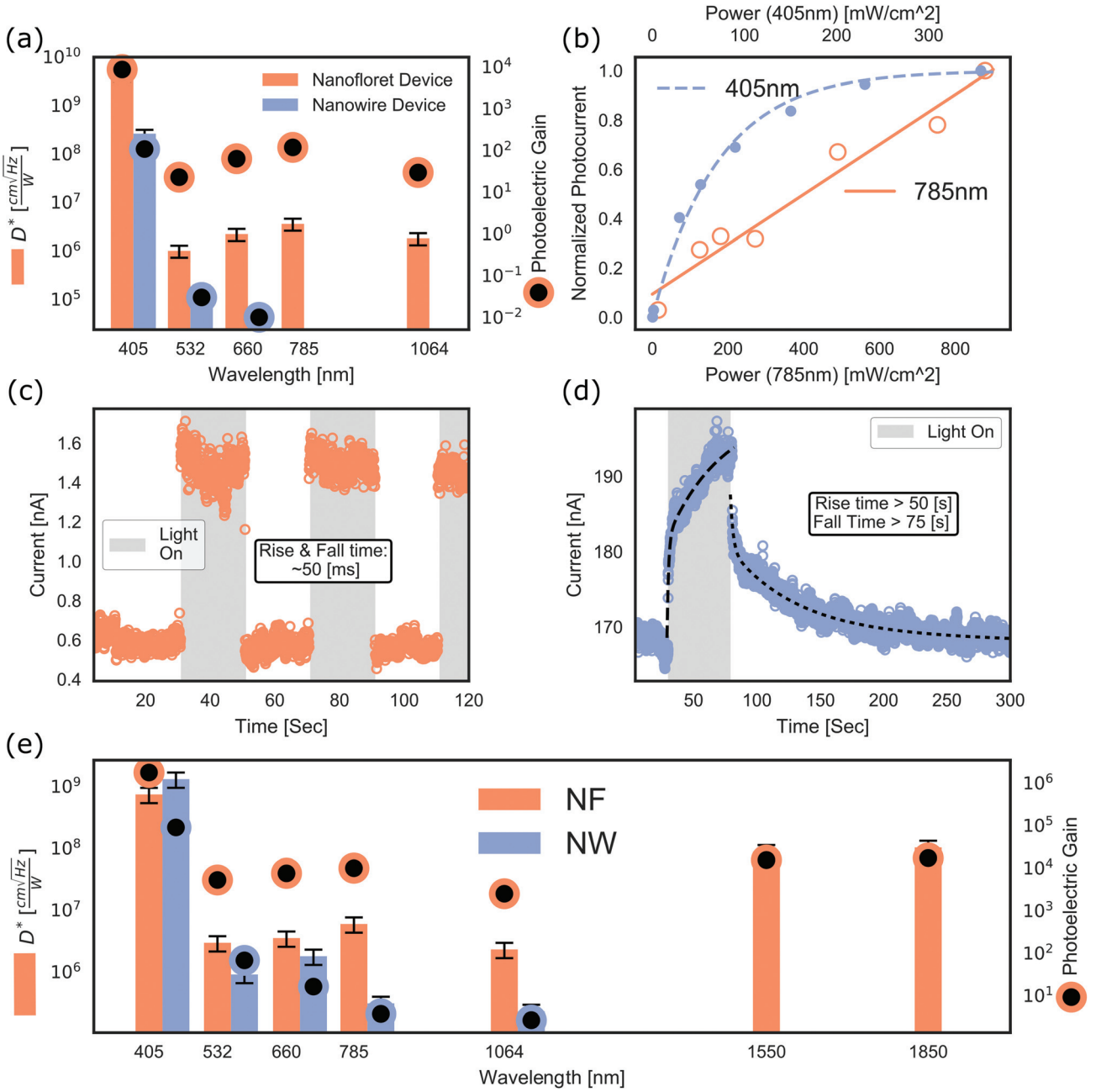

Fig. 2 (a) Specific detectivity, D^*, and photoelectric gain, g, as a function of wavelength for the NF and NW devices. At all wavelengths the NF device is superior to the NW device. A difference exists between the UV (405 nm) regime and the 532 nm to 1064 nm regime, suggesting for different photo-response mechanisms. (b) Photocurrent optical power dependence for illumination with 405 nm and 785 nm wavelengths; at 785 nm the dependence is linear while at 405 nm the response saturates in the power range we utilized. (c, d) Comparison between the photo-responses of (c) NF and (d) NW devices for illumination with a wavelength of 660 nm, where the rise and fall times of the NF device are shorter. The gray areas represent the *light on* periods. (e) The NF's device photo-response as a function of wavelength, for a device with pronounced surface states.

In addition to the difference in the magnitude of the photo-response, a significant decrease in the typical photo-response time scale is observed using the NF. This is displayed in Fig. 2c and d, where the change in the measured rise and fall times is presented for the 660 nm wavelength. The rise and fall times in the NW device are greater than 50 seconds, while for the NF device, the rise and fall times are about 50 milli-seconds. Such behavior was observed for all measured wavelengths and for several devices (see the ESI†) except for illumination at the 405 nm wavelength, which we also attribute to the different photo-response mechanisms. We ascribe the difference between the NF device and the unmodified SiGe nanowire to the LSPR mechanism owing to the Au-NF hybrid structure where the corrugated Au nanotip is coupled to the

tip of the semiconducting NW and bridges the nanostructure and macroscopic electrode, consisting of the device's current path.

Using a NF device, where the surface states are more pronounced, and the response time is slower (~10 seconds), a higher photo response wavelength cutoff of 1850 nm was achieved, this is displayed in Fig. 2e. In this type of device, the plasmons are also coupled to surface states enhancing the response (see the ESI† for an example).

Atom-probe tomography[33,34] (APT) was employed to provide high spatial resolution 3-D structures of the Au-NF metallic nanotip, this is displayed in Fig. 3. We utilized an Imago Scientific Instruments (Madison, Wisconsin) 4000× Si tomograph with a picosecond ultraviolet (wavelength = 355 nm) laser. Fig. 3(a) through (f) were constructed using the proximity histogram methodology, which we have developed and used extensively as an aid to interpreting 3-D atom-probe tomographic reconstructions.[35] This detailed information was utilized for understanding the broad range optical absorption measured for Au-NF, presented in Fig. 3, the photoresponse and for EM modeling of the Au-NF light absorption properties. In Fig. 3a–c, the APT data demonstrate that the metallic Au–Au clusters are separated by a thin dielectric layer, GeO_2, and that boundary is rough and corrugated with varying thickness ranging from 0 nm up to 3 nm. Therefore, the metallic nanotip should be treated as an array of Au nano-clusters separated by a dielectric interface layer rather than a continuous metallic nanotip, thus realizing a plasmonic nanometric metastructure.[36,37] Further analysis of the metallic nanotip–SC NW interface, displayed in Fig. 3d–f, proved that the nanotip is separated from the SC by GeO_2 and AuGe layers. The thin dielectric layer allows electrical transport, most likely due to electron tunneling, together with weak coupling, which supports the LSPR mechanism. Additionally, optical absorption data of Au-NF structures display an increase in optical absorption in the NIR–SWIR region with increasing NW diameter employed for the Au-NF synthesis. It is apparent that the optical absorption's magnitude is increased and red-shifted with increasing diameter. Additional experimental details of APT sample preparation and analysis of NWs and NFs were previously reported.[38,39]

To qualitatively understand the plasmonic response of the NF structure, a simple model was constructed following the atom-probe tomography (APT) results, which is presented in Fig. 4a. The model used gold nanoparticles (NPs) with equal radii (indicated by '*r*' in Fig. 4a) and equal edge-to-edge distances ('*d*' in Fig. 4a) between them located on top of a Ge NW and separated by GeO_2 (lighter blue in Fig. 4a). A commercial three-dimensional full-wave solver (CST Microwave Studio, Computer Simulation Technology GmbH, Darmstadt, Germany) based on the finite element method,[40] was used to simulate the electromagnetic fields, by illuminating the sample with a plane wave using the time domain solver. The extinction cross section (ECS) was calculated by integrating the electromagnetic far fields over a closed box around the model (see the ESI† for further details). The simulation results are

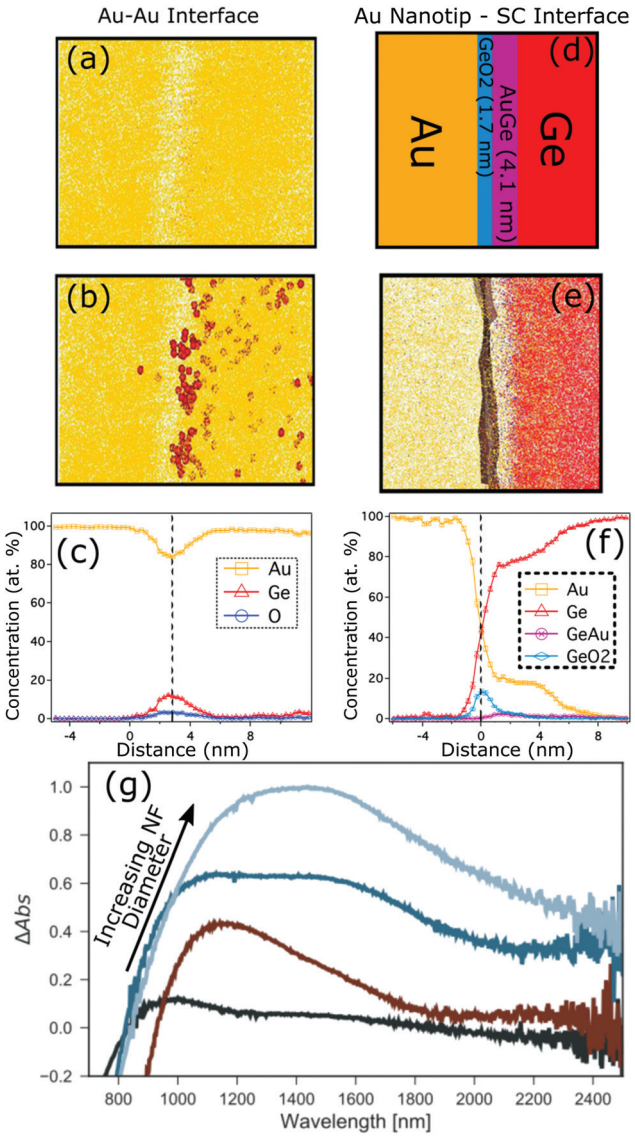

Fig. 3 Atom-probe tomographic (APT) results from a Au-NF tip region. (a, b) Atom-probe tomography reconstruction of the Au–Au interface. Colours correspond to the legend presented in (c). (c) Proximity histogram of the Au–Au interfaces shows gold clusters separated by an oxide layer. (d) Schematic of the Au–Ge interface. Colours correspond to the legend presented in (f). (e) Atom-probe tomography reconstruction of the Au–Ge interface (brown), indicated by a Ge 50 atomic% isoconcentration surface. (f) Proximity histogram of the Au tip–NW interface show a dielectric layer (GeO_2) and a AuGe layer formed between the tip and SC NW. Figures (a) through (f) were constructed using the proximity histogram methodology, which we have developed and used extensively as an aid to interpreting 3-D atom-probe tomographic reconstructions. (g) Optical absorption data of Au-NF with specified NW diameters (5, 10, 15 and 30 nm NF diameter); difference spectra obtained by subtraction 'NFs' minus 'NWs', displaying an increase in the absorption in the NIR–SWIR regime with increasing NW diameter.

presented in Fig. 4. Firstly, in Fig. 4b and c, it is apparent that as the edge-to-edge inter particle distance (d) is decreased, for the two different particle radii (r) 18 nm and 7 nm, the collective LSPR is redshifted, demonstrating that the NIR response

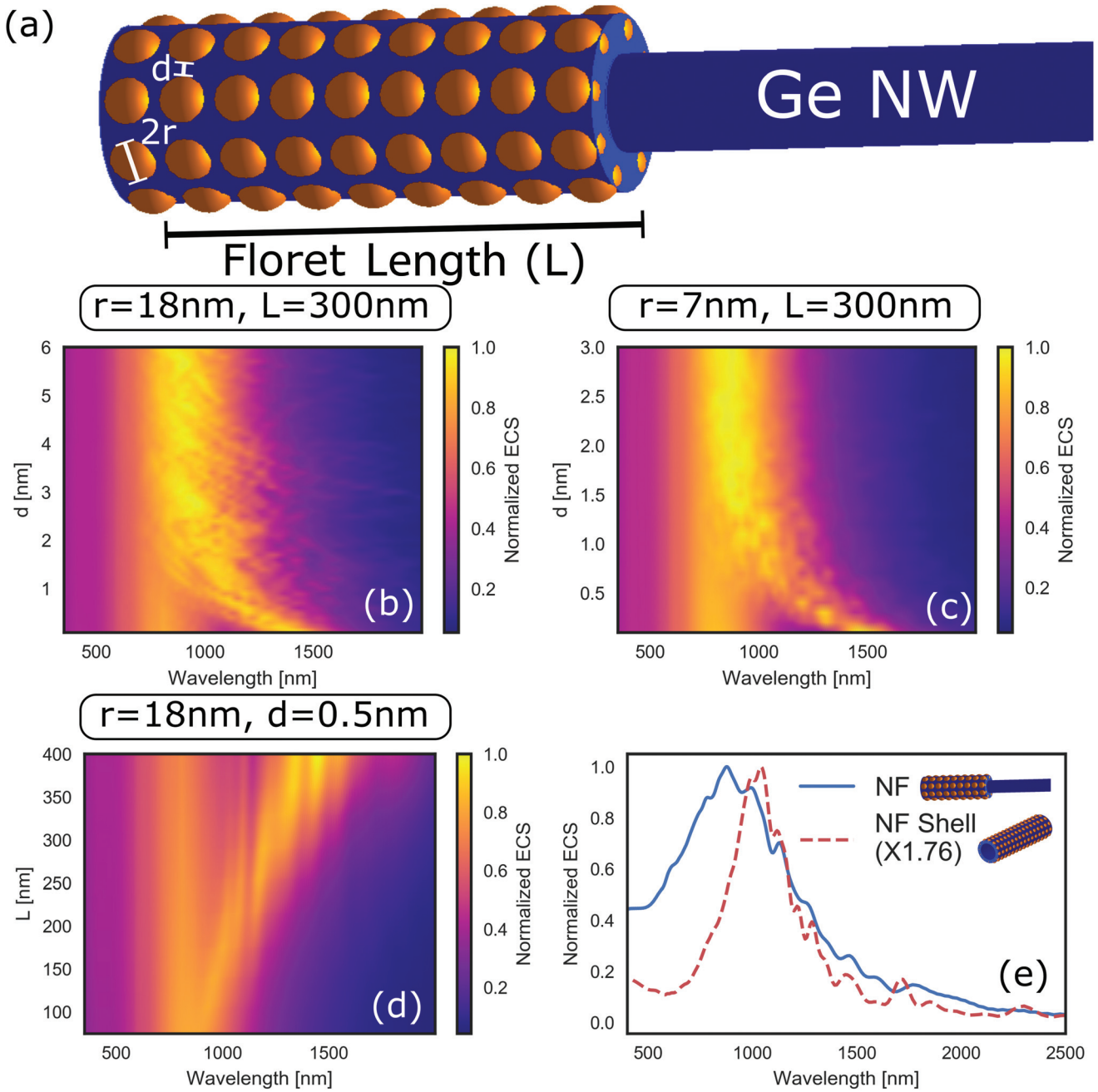

Fig. 4 EM simulation results for the Au-NF model using the CST Studio suite. (a) The NF model, showing the relevant simulation parameters: *d* – edge to edge inter-particle distance, *r* – NP radii and *L* – nanotip length; (b) normalized extinction cross section (ECS) as a function of wavelength and inter-particle distance, for 18 nm nanoparticle radius. The resonance is red shifted with decreasing inter-particle distance, *d*; (c) normalized ECS as a function of wavelength and inter-particle distance for a smaller nanoparticle radius, of 7 nm; (d) normalized ECS as a function of wavelength for different nano-floret lengths, *L*; and (e) representative calculated results for Au-NF and the metallic-shell ECS responses with 18 nm gold nanoparticles and an inter-particle distance of 1 nm. A clear enhancement in the long wavelength response is obtained for a simulated NF compared to only the NF shell, without coupling to the NW.

is indeed a collective effect of all the particles. Furthermore, both the device photoresponse and the measured absorbance show a response extending further to longer wavelengths (enhanced photoresponse at 1850 nm is shown in Fig. 2). The simulation resulted in an extinction cross section at relatively shorter wavelengths, which is expected considering the fact that below 1 nm edge-to-edge separation, electron tunneling becomes more probable and therefore charge transfer plasmon needs to be considered. In such a case, the plasmonic resonance is expected to be more red shifted,[41,42] which accounts for the measured results. Since most of the noise is coming from the junction itself, larger NF length (L) will

increase the absorption, thus the signal to noise ratio will also improve, which will lead to a detectivity improvement. Note that the charge transfer plasmons involve optical frequency electronic response, and there is no evidence that these are connected to the measured tunneling currents that are static. Another cause for a qualitative difference between the simulated and measured data is attributed to the heterogeneity and structural distribution of the gold nanotip and the clusters comprising it; this is manifested in gold cluster size distribution, distances and additional morphological heterogeneity. Secondly, for larger particle radii, the collective plasmonic resonance occurs at a larger edge-to-edge inter-particle distance (d). In Fig. 4d, the effect of increasing the total gold nanotip length ('L' in Fig. 4a) is displayed. This shows that increasing L results in red shifting and broadening of the plasmonic resonance, leading to results that are in better alignment with calculation for NP edge-to-edge (d) spacings that are not as small as with the smaller NF nanotip length (L) results. In Fig. 4e, the role of the semiconducting nanowire core is demonstrated, wherein the NF shell alone, that is, a hollow cylinder consists of gold NPs which are separated by a GeO_2 layer, the resonance is narrower compared to the full NF structure (the NF shell with the Ge NW core). It is important to emphasize that in addition to the red shifting of the ECS, a localized enhancement of the electromagnetic field is present exactly at the location of the tunnel junction, providing a mechanism for the observed photoconductive gain. Therefore, the device concept can, in principle, allow tuning the wavelength response enabling the realization of a simple, nanometric SWIR photodetector.

Simulations were performed on other models, which provided further insights; discussion on these is provided in the ESI.†

The electrical conductivity of the Ge NW devices was shown to be dominated by holes created by the thermal excitation of electrons from the valence band to the surface states located at the GeO_2 surface of the NWs[5,7,43–46] (Fig. 1a, top-right). Upon illumination, an electron–hole pair is created, followed by an electron drift, which becomes trapped in the surface states, thereby adding an additional hole to the valence band. The slow response time observed in the NW device (Fig. 2d) can be explained by the long lifetime of electrons in the surface states.

The crucial difference in D^* and g between the response at 405 nm and the different measured wavelengths is ascribed to a radiative transition in the Ge NWs at 3.2 eV (400 nm radiation), which is attributed to an internal transition in the Ge surface energy state structure.[47,48] Therefore, upon 405 nm illumination, electrons in lower surface energy states are excited to deeper surface states. This permits additional electrons to be thermally excited to the lower obtainable surface states resulting in additional holes and an increase in the electrical conductivity. The very long relaxation time of these deep energy states explains the larger gain, compared to the other wavelengths. The NF based photodetector showed an improved photoelectric gain compared to the NW photodetector for 405 nm wavelength as well, which can be attributed to the hot electrons[49] released and trapped surface states from the NF gold nanotip. Trapping into surface states also occurs at other wavelengths; however, since in that case the trapping is not into deep surface states, their contribution is less prominent compared to the contribution due to the enhanced localized plasmonic field.

Additionally, the NF-based detector has an improved response time. It was previously demonstrated, that in a Ge NW network device, a back-to-back Schottky junction exists between the crossed NWs, which improves drastically the response time of the photodetector.[50,51] In such cases, or in the case where a Schottky junction is created between the NW and the counter electrode, there is a small internal gain.[7] However, in the case of the NF device, three phenomena exist simultaneously, the plasmonic field enhancement, which effectively increases the amount of incident photons on the device and the tunneling photodetection mehanism[52,53] at the Au–Ge interface, alongside with plasmon induced hot electron injection from the gold nanotip,[28] which decreases the response time (Fig. 1a, top left). In this manner, both the response time and the gain are improved. For 405 nm, both the plasmonic enhancement and the deep surface state excitation occur, which explains the relatively longer response time, compared to the shorter response time at the other wavelengths, 50 ms. Furthermore, the two different mechanisms can also explain the power dependence presented in Fig. 2b; where for 405 nm illumination, the photocurrent is saturated at a high optical power, which is attributed to the saturation of surface traps. Whereas for 785 nm, the dependence is linear, suggesting a plasmonic origin.

Conclusions

In summary, we report a significant photocurrent gain that is achieved by coupling a localized plasmon of a nanoshell gold nanotip, placed at the edge of a semiconducting NW, to the NW. The fabrication process of the device relies on low-resolution photolithography for macroscopic contacts and on a bottom-up self-processing synthesis for the nano-scale structural motifs essential for generating the broad plasmonic response. Overall, the device fabrication process is simple and scalable. Furthermore, the tunneling junction between the gold nanotip and the semiconductor improves the response time drastically and the unique structure of the gold nanotip permits extending the response to the NIR–SWIR regime. Finally, we have previously demonstrated that this device is also sensitive to the presence of molecules at the Au-NF-electrode gap, therefore allowing electrical probing of light–molecule interactions.[32] The combined functionality of the device concept and the results presented herein open the possibility to realize a new class of photodetectors, which are simple to fabricate with controlled wavelength tunability and may be utilized as low-cost broad-band photodetectors as well as providing electrical and optical information at the molecular level for future applications.

Conflicts of interest

There are no conflicts to declare.

Acknowledgements

AT, ZS, LJL, DNS and RY acknowledge partial funding support from the United States – Israel Binational Science Foundation (grant number 2012088). The LEAP tomograph at NUCAPT was purchased and upgraded with grants from the NSF-MRI (DMR-0420532) and ONR-DURIP (N00014-0400798, N00014-0610539, N00014-0910781, N00014-1712870) programs. NUCAPT received support through the MRSEC program (NSF DMR-1720139) at the Materials Research Center and the SHyNE Resource (NSF ECCS-1542205), NUCAPT from the Initiative for Sustainability and Energy (ISEN), at Northwestern University. GCS thanks DOE grant DE-AC02-06CH11357. AZ would like to acknowledge the support of the Israeli Ministry of Science, Technology and Space.

References

1 Y. Li, F. Qian, J. Xiang and C. M. Lieber, *Mater. Today*, 2006, **9**, 18–27.
2 R. R. LaPierre, M. Robson, K. M. Azizur-Rahman and P. Kuyanov, *J. Phys. D: Appl. Phys.*, 2017, **50**, 123001.
3 L. VJ, J. Oh, A. P. Nayak, A. M. Katzenmeyer, K. H. Gilchrist, S. Grego, N. P. Kobayashi, S. Y. Wang, A. A. Talin, N. K. Dhar and M. S. Islam, *IEEE J. Sel. Top. Quantum Electron.*, 2011, **17**, 1002–1032.
4 N. Guo, W. Hu, L. Liao, S. Yip, J. C. Ho, J. Miao, Z. Zhang, J. Zou, T. Jiang, S. Wu, X. Chen and W. Lu, *Adv. Mater.*, 2014, **26**, 8203–8209.
5 Y. H. Ahn and J. Park, *Appl. Phys. Lett.*, 2007, **91**, 162102.
6 J. Miao, W. Hu, N. Guo, Z. Lu, X. Zou, L. Liao, S. Shi, P. Chen, Z. Fan, J. C. Ho, T.-X. Li, X. S. Chen and W. Lu, *ACS Nano*, 2014, **8**, 3628–3635.
7 C.-J. Kim, H.-S. Lee, Y.-J. Cho, K. Kang and M.-H. Jo, *Nano Lett.*, 2010, **10**, 2043–2048.
8 X. Yan, B. Li, Y. Wu, X. Zhang and X. Ren, *Appl. Phys. Lett.*, 2016, **109**, 053109.
9 O. Hayden, R. Agarwal and C. M. Lieber, *Nat. Mater.*, 2006, **5**, 352–356.
10 Y. Gu, J. P. Romankiewicz, J. K. David, J. L. Lensch and L. J. Lauhon, *Nano Lett.*, 2006, **6**, 948–952.
11 C. Soci, A. Zhang, B. Xiang, S. A. Dayeh, D. P. R. Aplin, J. Park, X. Y. Bao, Y. H. Lo and D. Wang, *Nano Lett.*, 2007, **7**, 1003–1009.
12 A. L. Falk, F. H. L. Koppens, C. L. Yu, K. Kang, N. de L. Snapp, A. V. Akimov, M.-H. Jo, M. D. Lukin and H. Park, *Nat. Phys.*, 2009, **5**, 475.
13 K. M. Evans, P. Zolotavin and D. Natelson, *ACS Photonics*, 2015, **2**, 1192–1198.
14 M. S. Shishodia and A. G. Unil Perera, *J. Appl. Phys.*, 2011, **109**, 043108–.
15 M. L. Brongersma, *Proc. IEEE*, 2016, **104**, 2349–2361.
16 S. Schlücker, *Angew. Chem., Int. Ed.*, 2014, **53**, 4756–4795.
17 M. J. Ashley, M. R. Bourgeois, R. R. Murthy, C. R. Laramy, M. B. Ross, R. R. Naik, G. C. Schatz and C. A. Mirkin, *J. Phys. Chem. C*, 2018, **122**, 2307–2314.
18 R. L. M. Gieseking, J. Lee, N. Tallarida, V. A. Apkarian and G. C. Schatz, *J. Phys. Chem. Lett.*, 2018, **9**, 3074–3080.
19 B. Zheng, H. Zhao, B. Cerjan, S. Yazdi, E. Ringe, P. Nordlander and N. J. Halas, *Appl. Phys. Lett.*, 2018, **113**, 101105.
20 Y. Paltiel, A. Aharoni, U. Banin, O. Neuman and R. Naaman, *Appl. Phys. Lett.*, 2006, **89**, 033108.
21 A. De Luca, M. P. Grzelczak, I. Pastoriza-Santos, L. M. Liz-Marzán, M. La Deda, M. Striccoli and G. Strangi, *ACS Nano*, 2011, **5**, 5823–5829.
22 X. DANG, J. QI, M. T. KLUG, P.-Y. CHEN, D. S. YUN, N. X. FANG, P. T. HAMMOND and A. M. BELCHER, *Nano Lett.*, 2013, **13**, 637–642.
23 A. Akbari and P. Berini, *Appl. Phys. Lett.*, 2009, **95**, 021104.
24 C. Scales and P. Berini, *IEEE J. Quantum Electron.*, 2010, **46**, 633–643.
25 I. Goykhman, B. Desiatov, J. Khurgin, J. Shappir and U. Levy, *Nano Lett.*, 2011, **11**, 2219–2224.
26 M. W. Knight, H. Sobhani, P. Nordlander and N. J. Halas, *Science*, 2011, **332**, 702–704.
27 K. C. Balram, R. M. Audet and D. A. B. Miller, *Opt. Express*, 2013, **21**, 10228–10233.
28 A. Sobhani, M. W. Knight, Y. Wang, B. Zheng, N. S. King, L. V. Brown, Z. Fang, P. Nordlander and N. J. Halas, *Nat. Commun.*, 2013, **4**, 1643.
29 S.-W. Jee, K. Zhou, D.-W. Kim and J.-H. Lee, *Nano Convergence*, 2014, **1**, 29.
30 L. Cao, J. S. White, J.-S. Park, J. A. Schuller, B. M. Clemens and M. L. Brongersma, *Nat. Mater.*, 2009, **8**, 643–647.
31 O. Hazut, S. Waichman, T. Subramani, D. Sarkar, S. Dash, T. Roncal-Herrero, R. Kröger and R. Yerushalmi, *J. Am. Chem. Soc.*, 2016, **138**, 4079–4086.
32 A. Ziv, A. Tzaguy, O. Hazut, S. Yochelis, R. Yerushalmi and Y. Paltiel, *RSC Adv.*, 2017, **7**, 25861–25866.
33 D. N. Seidman, *Annu. Rev. Mater. Res.*, 2007, **37**, 127–158.
34 D. N. Seidman and K. Stiller, *MRS Bull.*, 2009, **34**, 717–724.
35 O. C. Hellman, J. A. Vandenbroucke, J. Rüsing, D. Isheim and D. N. Seidman, *Microsc. Microanal.*, 2000, **6**, 437–444.
36 J. A. Schuller, E. S. Barnard, W. Cai, Y. C. Jun, J. S. White and M. L. Brongersma, *Nat. Mater.*, 2010, **9**, 193–204.
37 M. R. Bourgeois, A. T. Liu, M. B. Ross, J. M. Berlin and G. C. Schatz, *J. Phys. Chem. C*, 2017, **121**, 15915–15921.
38 Z. Sun, O. Hazut, R. Yerushalmi, L. J. Lauhon and D. N. Seidman, *Ultramicroscopy*, 2018, **184**, 225–233.
39 Z. Sun, A. Tzaguy, O. Hazut, L. J. Lauhon, R. Yerushalmi and D. N. Seidman, *Nano Lett.*, 2017, **17**, 7478–7486.
40 B. Szabó, B. A. Szabo and I. Babuška, *Finite Element Analysis*, John Wiley & Sons, 1991.
41 J. H. Yoon, Y. Zhou, M. G. Blaber, G. C. Schatz and S. Yoon, *J. Phys. Chem. Lett.*, 2013, **4**, 1371–1378.

42 R. Esteban, A. G. Borisov, P. Nordlander and J. Aizpurua, *Nat. Commun.*, 2012, **3**, 825.
43 T. Nishimura, K. Kita and A. Toriumi, *Appl. Phys. Lett.*, 2007, **91**, 123123.
44 T. Hanrath and B. A. Korgel, *J. Phys. Chem. B*, 2005, **109**, 5518–5524.
45 H.-K. Seong, E.-K. Jeon, M.-H. Kim, H. Oh, J.-O. Lee, J.-J. Kim and H.-J. Choi, *Nano Lett.*, 2008, **8**, 3656–3661.
46 L. Zhang, R. Tu and H. Dai, *Nano Lett.*, 2006, **6**, 2785–2789.
47 A. Prakash, S. Maikap, S. Z. Rahaman, S. Majumdar, S. Manna and S. K. Ray, *Nanoscale Res. Lett.*, 2013, **8**, 220.
48 X. C. Wu, W. H. Song, B. Zhao, Y. P. Sun and J. J. Du, *Chem. Phys. Lett.*, 2001, **349**, 210–214.
49 E. A. Sprague-Klein, B. Negru, L. R. Madison, S. C. Coste, B. K. Rugg, A. M. Felts, M. O. McAnally, M. Banik, V. A. Apkarian, M. R. Wasielewski, M. A. Ratner, T. Seideman, G. C. Schatz and R. P. Van Duyne, *J. Am. Chem. Soc.*, 2018, **140**, 10583–10592.
50 C. Yan, N. Singh, H. Cai, C. L. Gan and P. S. Lee, *ACS Appl. Mater. Interfaces*, 2010, **2**, 1794–1797.
51 V. Dhyani and S. Das, *Semicond. Sci. Technol.*, 2017, **32**, 055008.
52 S. Faris, T. Gustafson and J. Wiesner, *IEEE J. Quantum Electron.*, 1973, **9**, 737–745.
53 M. Heiblum, S. Wang, J. Whinnery and T. Gustafson, *IEEE J. Quantum Electron.*, 1978, **14**, 159–169.